

Bifurcations and phase-space structures in KCN molecular system

F. Revuelta,¹ F. J. Arranz,¹ R. M. Benito,¹ and F. Borondo²

¹*Grupo de Sistemas Complejos, Escuela Técnica Superior de Ingeniería Agronómica,
Alimentaria y de Biosistemas, Universidad Politécnica de Madrid,
Avenida Puerta de Hierro 2-4, 28040 Madrid, Spain.*

²*Departamento de Química, Universidad Autónoma de Madrid, Cantoblanco, 28049 Madrid, Spain.*

In this work, we analyze the evolution of the phase-space structures of KCN molecular system as a function of the vibrational energy using Lagrangian descriptors. For low energies, the motion is mostly regular around the absolute minimum of the potential energy surface. As the energy increases, the phase space combines regions with regular and chaotic motion, a difference that is well captured by the Lagrangian descriptors. We show that the dynamics is mostly governed by the invariant manifolds of the stretch periodic orbits located at the top of one of the energetic barriers of the system. Furthermore, we show a perfect agreement between the bifurcation theory and the differences observed in the phase-space structures as the vibrational energy is modified. The accuracy of our calculations is also assessed by explicit comparison with the invariant manifolds computed using linear dynamics.

Keywords: Bifurcation, Molecular vibration, Invariant manifold, Lagrangian descriptors.

I. INTRODUCTION

Periodic orbits (POs) are trajectories that describe periodic cycles [1], i. e., they return to the same point after a time named as the period of the PO. Although typical POs themselves occupy a finite region of phase space, they are surrounded by geometrical structures which can significantly influence the system’s global dynamics [2, 3]. On the one hand, stable POs are resilient to disturbances and return to their original path after suffering a small perturbation. They are surrounded by invariant tori where quasiperiodic motion occurs. On the other hand, unstable POs exhibit, conversely, different behavior: small perturbations increase exponentially over time. Moreover, they can be embedded within the chaotic sea without presenting the usual erratic motion shown by generic chaotic trajectories. Finally, marginally stable POs are on the boundary between stability and instability, as small perturbations do not grow or shrink over time.

When a nonlinear system is manipulated by changing some of its parameters (such as energy, mass, shape, . . .), the POs can undergo dramatic changes. Bifurcations [4] can lead to the emergence of new POs, thereby drastically altering the phase-space structure. Changes in the stability of POs can profoundly impact system dynamics [1]; for example, a stable PO may become marginally stable and eventually unstable, or an unstable PO can become, first, marginally stable, and then stable. Extensive literature, spanning from nonlinear oscillators [5] to fluid dynamics [6] and celestial mechanics [2], illustrates these phenomena. At the same time, when bifurcations occur, the invariant geometrical objects responsible for the dynamics can be distorted, disappear, or new ones may emerge.

Several tools have been developed over time in order to analyze phase-space structures. In the case of dynamical systems with 2 degrees of freedom (dofs), the Poincaré surface of section (PSS) remains a cornerstone [7]. This tool allows the unambiguous identification of invariant tori and efficiently determines whether motion is regular or chaotic. The Lyapunov exponent is another remarkable chaos indicator also applicable in systems with more than 2 dofs [1]. However, its calculation is computationally demanding. Therefore, alternatives have been developed, such as the fast Lyapunov indicator [8, 9], the small-alignment index [10, 11] and the mean exponential growth factor of nearby orbits [12, 13], among others. Lagrangian descriptors (LDs) [14–17] also offer an attractive approach to unveil the underlying phase-space structures. They have been successfully applied in various fields such as oceanic [17] and cardiovascular flows [18], chemical [19, 20] and molecular systems [21–24], and chaotic maps [15, 25–27] and billiards [28]. These major tools, along with others, enable the study of the broad field of nonlinear dynamics, forming the core of chaos theory. Furthermore, they can be applied to study molecular vibrations as vibrational motion takes place when atomic particles sojourn the potential energy surface (PES) exerted by the electronic structure [29–31]. This is especially interesting when the vibration energy is well above the ground-state energy since then the non-negligible anharmonic terms in the PES make normal mode analysis unsuitable [32].

The standard description of molecular systems typically lies on the Born-Oppenheimer or adiabatic approximation [30, 31]. Within this approach, the motion of the atomic nuclei is separated from that of the electrons, due to their significant mass difference, which spans at least three orders of magnitude. Consequently, the PES associated with the electrons is computed for each position of the atomic nuclei. The computation of the PES often requires the application of advanced *ab-initio* quantum chemistry tools [33], something usually very time-consuming and computationally demanding. The atomic nuclei undergo vibrational motion on the PES created by the electrons. For small energies, atomic nuclei simply vibrate around the equilibrium positions found at the PES minima. However, when the energy is sufficiently high, nuclei can explore larger regions of the PES, rendering other more complex phenomena such as isomerization. This structural change in the molecule can have significant implications in its chemical properties and stability [30, 31]. The typically strong anharmonicities in the PES can make this process extraordinary complicated. Nevertheless, concepts and tools developed within the fields of nonlinear mechanics and dynamical systems theory can greatly facilitate the study [34]. For example, they can be used to establish whether nuclei present regular or irregular motion. Moreover, they can be applied to identify the underlying geometrical structures that determine nuclear motion, as well as to identify the reaction mechanism that is responsible, among others, for molecular isomerization [34]. Following this mathematical perspective, in configurations close to the PES minima, nuclei simply vibrate because of the existence of invariant tori which force the motion to be regular within a certain region of phase space. As a consequence, the nuclei can show periodic or quasiperiodic motion, depending on where they are located on a regular PO or not. As the energy increases, according to the Poincaré-Birkhoff theorem [35], the occurrence of bifurcations leads to the appearance of new POs, while invariant tori break down, as prescribed by the Kolmogorov-Arnold-Moser theorem [7, 36]. Consequently, the route for chaotic motion is opened, making the dynamics much more intricate. Still, just like in any other generic nonlinear system, stable and unstable POs can be found, corresponding to situations where the nuclei exhibit periodic motion. Moreover, the motion of the nuclei when located in the vicinity of these objects can be also well understood. On the one hand, when located close to a stable

PO, the nuclei describe quasiperiodic vibrational motion due to the existence of invariant tori. On the other hand, when found in the vicinity of an unstable PO, the motion of nuclei is more involved but it can be accurately described within a linear approximation. Nuclei exponentially separate for the reference PO in the directions of the unstable manifolds. At larger distances, the manifolds fold and the linear approximation breaks down, but the importance of the invariant manifolds is still substantial in the system dynamics.

In this work, we investigate the phase-space structures responsible for the intricate nonlinear dynamics of KCN molecular system using LDs. For very low energies, we show the existence of a single regular PO associated with the vibrational motion of K atomic nuclei around the absolute minimum of the PES. As the energy increases, the primary PO experiences a series of (infinite) bifurcations. The most dramatic one occurs at a relative low energy, where the PO loses stability, triggering the emergence of another stable PO. This newly formed stable PO remains stable within a reasonably small range of energy until another bifurcation arises. For higher energies, the global dynamics are primarily governed by the invariant manifolds that emerge from unstable POs located at the top of one of the energetic barriers. This phenomenon is well captured by the LDs. This secondary PO also suffers a series of bifurcations, which we similarly analyzed. We discuss the corresponding changes in the phase-space structures, with special attention given to the unexpected stabilization process of the PO as the energy is modified. At a certain bifurcation energy, the secondary PO transforms into a stable orbit, resulting in regular motion of K atomic nuclei within a small region of phase space. This stabilization process is well captured by the LDs, and is in agreement with dynamical systems theory. We illustrate that the bifurcation occurs when the stable and unstable manifolds of the reference POs are distorted and degenerate at the bifurcation energy. As the energy increases, the size of the stability region, which is associated with invariant tori, first increases, and then reduces until it disappears, causing the PO to return to an unstable state. We briefly discuss some of the bifurcations that occur in between, demonstrating excellent agreement between the LDs computations and dynamical systems theory. To conclude, in order to strengthen the accuracy of LDs, we explicitly compare the LDs results with numerically-computed invariant manifolds.

The structure of the paper is as follows. Following this introduction, we provide a brief overview of the KCN molecular system under study in Sec. II. In Sec. III, we introduce the methods and tools used to analyze the system. Section IV presents the results obtained and the corresponding discussion. Finally, we conclude the article with a summary in Sec. V.

II. SYSTEM

In this work, we study the vibrational motion of potassium cyanide molecular system, KCN. In the rotationless setting, the configuration of this triatomic molecule can be characterized using the Jacobi coordinates shown in the insets of Fig. 1(b). Here, R is the radial distance between the potassium atom and the center of mass of the CN group, and θ is the angle that the previous radius forms with the longitudinal axis of CN. Due to the triple bond that bounds carbon and nitrogen atoms, this vibrational mode can be effectively decoupled from the rest of the molecule. Thus, in practice, the C-N distance can be set equal to the equilibrium value $r_{\text{eq}} = 2.224$ a.u. Then, the system can be accurately described by using the following 2-dofs Hamiltonian

$$\mathcal{H}(P_R, P_\theta, R, \theta) = \frac{P_R^2}{2\mu_1} + \frac{P_\theta^2}{2} \left(\frac{1}{\mu_1 R^2} + \frac{1}{\mu_2 r_{\text{eq}}^2} \right) + V(R, \theta), \quad (1)$$

where P_R and P_θ are the conjugate momenta to R and θ coordinates, $\mu_1 = m_K(m_C + m_N)/(m_K + m_C + m_N)$ and $\mu_2 = m_C m_N/(m_C + m_N)$ are the reduced masses for K-CN and CN groups, respectively, and $V(R, \theta)$ is the Bohr-Oppenheimer PES that determines the surrounds of the atomic nuclei due to the electronic structure.

Figure 1(a) shows as a contour plot the fundamental domain ($0 \leq \theta \leq \pi$ rad) of the *ab-initio* PES taken from Ref. [37]. As can be seen, the PES presents two minima (black circles) and two saddle points (black crosses), which are joined by the minimum energy path (MEP) $R_{\text{MEP}}(\theta)$, plotted superimposed as a dashed blue line. These critical points are more clearly visible in Fig. 1(b), where the profile of the PES along the MEP is represented. For $\theta = 0$ and π rad, respectively, the molecule forms the colinear configurations K-CN (left) and CN-K (right) shown at the bottom of Fig. 1(b). The configurations for the intermediate saddle and minimum points are also sketched in the insets of Fig. 1(b).

III. METHODS

In this section, we report on the methods used to conduct our study. First, we summarize in Sec. III A the tool used to identify the phase-space structures that are responsible for the dynamics of the molecule under study: the

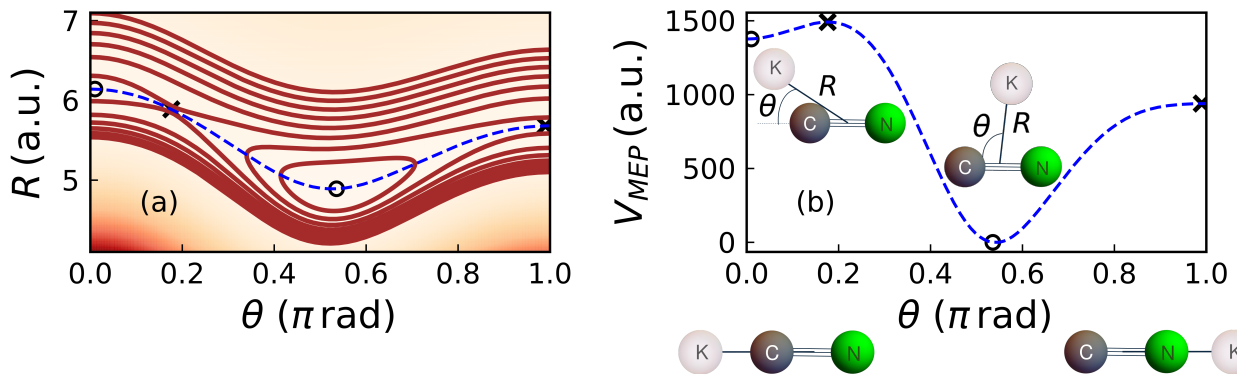


Figure 1: KCN molecular system. (a) Fundamental domain of the *ab-initio* potential energy surface as a function of the Jacobi coordinates R and θ . The continuous brown lines show the equipotential lines for $V(R, \theta) = 500, 1000, \dots, 3500, 4000 \text{ cm}^{-1}$. The potential minima (black circles) and the saddle points (black crosses) are joined by the superimposed minimum energy path (dashed blue line). (b) Profile of the potential energy surface along the minimum energy path (dashed blue line) with the corresponding critical points (black symbols). Insets: Sketches of the configuration of KCN molecule at the left saddle point and at the potential minimum with the Jacobi coordinates. Bottom: Sketches of the colinear configurations of the molecule for $\theta = 0 \text{ rad}$ (left), and $\theta = \pi \text{ rad}$ (right).

LDs. Second, we briefly discuss the linearized dynamics around periodic orbits in Sec. III B, and discuss the changes in stability as a function of the energy, including the occurrence of bifurcations.

A. Lagrangian descriptors

The tool selected to analyze the phase-structures that are responsible for the highly nonlinear dynamics of KCN are LDs. For a system with N dofs, LDs are defined as [15]

$$M_{\pm} = \pm \sum_{i=1}^{2N} \int_0^{\pm\tau} |\dot{z}_i(t)|^p dt, \quad (2)$$

with $0 < p \leq 1$, and $\mathbf{z}(t)$ a symplectic coordinate, that solves the equations of motion

$$\dot{z}_i = \mathbf{J} \frac{\partial \mathcal{H}}{\partial z_i}, \quad \text{with } \mathbf{J} = \begin{pmatrix} \mathbf{0}_{N \times N} & \mathbf{I}_{N \times N} \\ -\mathbf{I}_{N \times N} & \mathbf{0}_{N \times N} \end{pmatrix}. \quad (3)$$

As will be shown below in section IV, M_- , i.e., the integration backwards in time of Eq. (2), unveils the unstable manifolds of a dynamical system, whilst M_+ , i.e., the integration forward in time, unravels the stable manifolds. Thus, the sum $M_- + M_+$ can be used to identify the homoclinic and heteroclinic tangle as it accounts for the stable and unstable manifolds at the same time.

For the case study, $N = 2$ and $\mathbf{z}(t) = (R(t), \theta(t), P_R(t), P_\theta(t))$. We have already shown elsewhere [24] that a value of $p = 0.4$ and an integration time of $\tau = 2 \times 10^4 \text{ a.u.}$ seem to be adequate for triatomic molecular systems [22, 23] like the one under study.

B. The linearized motion

The motion in the close vicinity of a PO can be described within a linear approximation [1]. Then, for given a reference PO $\mathbf{z}_{\text{PO}}(t)$ with the initial condition $\mathbf{z}_{\text{PO}}(0)$, the time evolution of an initial condition $\mathbf{z}(0) = \mathbf{z}_{\text{PO}}(0) + \delta\mathbf{z}(0)$, with $\delta\mathbf{z}(0)$ sufficiently small, can be characterized by the time evolution of the vector $\delta\mathbf{z}(t)$ that accounts for the distance to the reference PO, which is given by

$$\delta\mathbf{z}(t) = \mathcal{M}(t)\delta\mathbf{z}(0), \quad (4)$$

where $\mathcal{M}(t)$ is a Jacobian matrix that accounts for the linearized flow along the PO and satisfies that $\dot{\mathcal{M}}(t) = \mathcal{L}\mathcal{M}(t)$, with $\mathcal{L} = \mathbf{J} \frac{\partial^2 \mathcal{H}}{\partial z^2}$, being \mathbf{J} given by Eq. (3), and $\mathcal{M}(0) = \mathbf{I}$. Furthermore, due to Liouville theorem [7], the determinant of the monodromy matrix always equals one.

After one period of time $\mathbf{z}_{\text{PO}}(T) = \mathbf{z}_{\text{PO}}(0)$, the Jacobian matrix $\mathcal{M}(T)$ is known as the *monodromy matrix* of the PO. The dimension of this matrix is equal to the number of dofs. Nonetheless, all the nontrivial information is solely portrayed by the transversal components to the PO. For the case study, these components define a plane. The corresponding *transversal monodromy matrix* $\mathcal{M}_\perp^\perp(T)$ has, as a consequence, dimension 2.

1. Stability of periodic orbits and bifurcations

Since the determinant of $\mathcal{M}_\perp^\perp(T)$ equals one, the corresponding eigenvalues can be written as

$$\mu_\pm = \frac{\text{Tr}(\mathcal{M}_\perp^\perp)}{2} \pm i \sqrt{1 - \left(\frac{\text{Tr}(\mathcal{M}_\perp^\perp)}{2}\right)^2}, \quad (5)$$

so that $\mu_+ \mu_- = 1$, and $\mu_+ + \mu_- = \text{Tr}(\mathcal{M}_\perp^\perp)$ is a real number.

For stable POs, the two eigenvalues are complex conjugates on the unit circle $\mu_\pm = e^{\pm i\sigma}$, with $\sigma \in \mathbb{R}$, and then $\text{Tr}(\mathcal{M}_\perp^\perp) = 2 \cos \sigma$. In this case, $|\text{Tr}(\mathcal{M}_\perp^\perp)| < 2$. For unstable POs, the two eigenvalues are real reciprocals $\mu_+ = \mu_-^{-1}$, and then $|\mu_\pm| = e^{\pm\sigma}$. We have, as a consequence, that $|\text{Tr}(\mathcal{M}_\perp^\perp)| = 2 \cosh \sigma$, and $|\text{Tr}(\mathcal{M}_\perp^\perp)| > 2$. When $\mu_+ > 1$, both eigenvalues and the trace are positive; In this situation, the unstable PO is *hyperbolic*. Contrarily, when $\mu_+ < -1$, both eigenvalues and the trace are negative, and the PO is called *hyperbolic with reflection*. In any case, the inverse of the Floquet exponents defined as $\lambda_\pm = \frac{\pm\sigma}{T}$ determines the characteristic time scale for the linearized motion. Finally, when the two eigenvalues of \mathcal{M}_\perp^\perp are equal $\mu_+ = \mu_- = \pm 1$, and $|\text{Tr}(\mathcal{M}_\perp^\perp)| = 2$. In this limiting case, a *marginally stable PO* is found [38].

For POs of n -period, with $n = 1, 2, \dots$, the previous reasoning remains valid by substitution of \mathcal{M}_\perp^\perp by $\mathcal{M}_n^\perp = (\mathcal{M}_\perp^\perp)^n$. Then, $\text{Tr}(\mathcal{M}_n^\perp) = 2 \cos(n\sigma) = 2 \cos[\arccos(\text{Tr}(\mathcal{M}_\perp^\perp)/2)]$, or $\text{Tr}(\mathcal{M}_n^\perp) = 2 \cosh(n\sigma) = 2 \cosh[\text{arccosh}(\text{Tr}(\mathcal{M}_\perp^\perp)/2)]$, depending on whether the PO is stable or unstable, respectively. When a bifurcation takes place, a new n -period PO emerges or disappears, something that requires that $|\text{Tr}(\mathcal{M}_n^\perp)| = 2$, a condition that is fulfilled when

$$\text{Tr}(\mathcal{M}_\perp^\perp) = 2 \cos\left(\frac{2\pi m}{n}\right), \quad (6)$$

with m an integer such that the cosine in Eq. (6) is π -modulus. Let us conclude by remarking that unstable POs do not bifurcate, i.e., they do not render new POs, but they can change their stability from unstable to stable when the trace of their corresponding transversal matrix equals 2.

In summary, the eigenvalues of $\mathcal{M}_\perp^\perp(T)$ given by Eq. (5) encode all the information necessary to establish whether a PO is stable, unstable or marginally stable, and bifurcations occur when Eq. (6) is fulfilled.

IV. RESULTS

This section describes the main findings of our study. For this purpose, we show plots with the LDs computed for pairs of initial conditions (ϑ, P_ϑ) at the PSS [7] defined along the MEP (MEP-PSS) [39], where $R = R_{\text{MEP}}(\theta)$, as

$$\vartheta = \theta, \quad (7a)$$

$$P_\vartheta = P_\theta + P_R \frac{dR_{\text{MEP}}(\theta)}{d\theta}, \quad (7b)$$

for $P_R < 0$. The MEP-PSS is the most likely, then useful, PSS to be crossed by a generic trajectory as the MEP is the lowest energetic path that connects the system minima. Thus, in what follows we will compute the LDs as defined in Eq. (2) for uniform sets of initial conditions located on the MEP-PSS with different vibrational energies. Next, we present in Secs. IV A and IV B the results for low and high vibrational energies, respectively.

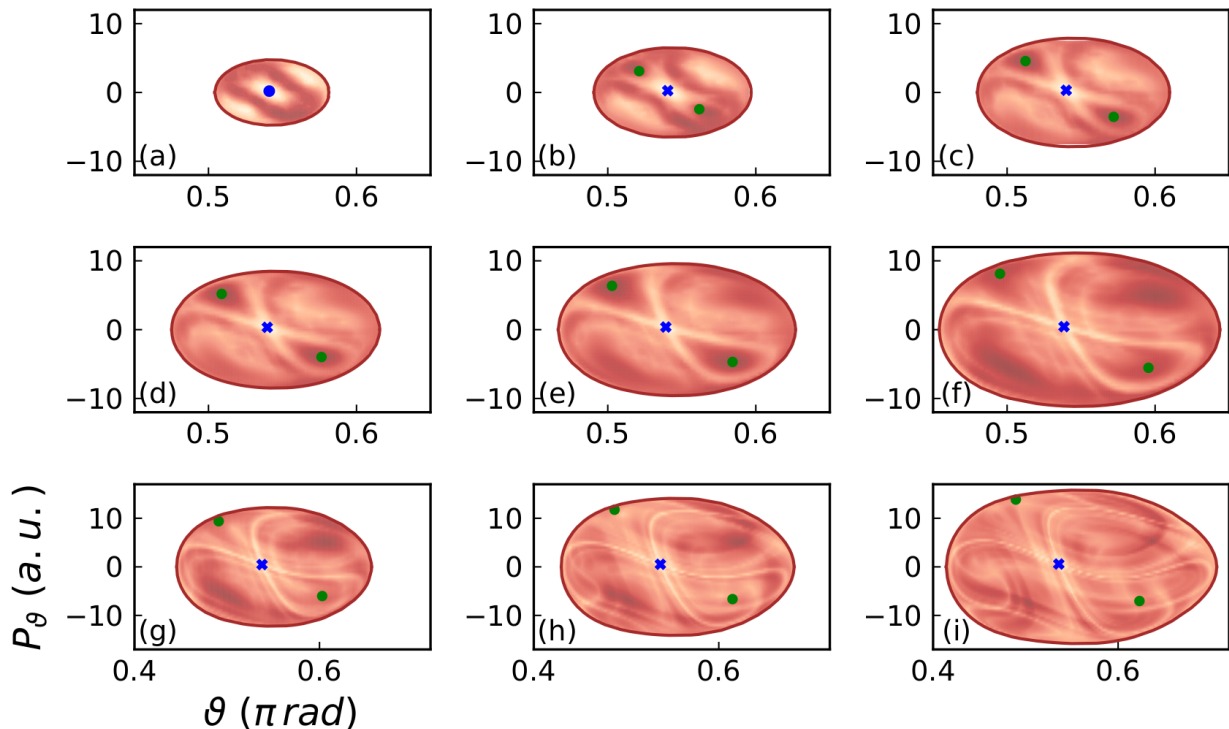


Figure 2: Sum $M_- + M_+$ of the Lagrangian descriptors (2) for $p = 0.4$ and $\tau = 2 \times 10^4$ a.u., and vibrational energies equal to (a) 45 cm^{-1} , (b) 85 cm^{-1} , (c) 125 cm^{-1} , (d) 145 cm^{-1} , (e) 185 cm^{-1} , (f) 250 cm^{-1} , (g) 300 cm^{-1} , (h) 400 cm^{-1} , and (i) 500 cm^{-1} . The blue symbols mark the positions of the elliptic (circle) and hyperbolic (cross) fixed points associated with the 1:1 resonance, and the green circles those of the elliptic fixed points related to the 1:2 resonance.

A. Phase-space structures for low energies

Figure 2 shows the LDs defined in Eq. (2) for a uniform set of initial conditions at the MEP-PSS. As in Ref. [24], the value of the integration time has been set equal to $\tau = 2 \times 10^4$ a.u. (see discussion below on its appropriateness). As expected, the energetically accessible region of phase space increases with the energy, and so does the accessible area of the MEP-PSS. For the lowest-lying energy considered, $E = 45 \text{ cm}^{-1}$, the LDs shown in Fig. 2(a) are slow varying functions, which shows the existence of regular motion. Notice the *donut*-like structure around the central point that is recognizable in the plot. This structure corresponds to a series of invariant tori that separate the motion within the inner region from the motion within the outer part. Notice the blue circle in the center of the plot $(\vartheta, P_\vartheta) = (0.541, 0.196) (\pi \text{ rad}, \text{a.u.})$, which marks the position of the elliptic fixed point associated with a primary stretch K-CN PO. This trajectory is stable and has $\theta(t) \approx \vartheta_{\text{PO}} = 0.541\pi \text{ rad}$. Furthermore, its radial, and angular frequencies, ω_R and ω_θ , are equal, indicating a $\omega_R : \omega_\theta = 1:1$ resonance.

For $E = 45.9 \text{ cm}^{-1}$, the previous stable PO bifurcates, resulting a central unstable PO and a neighboring stable PO. As the energy increases, the stable PO separates from the central region. Figure 2(b) shows the LDs for $E = 85 \text{ cm}^{-1}$, an energy where the two POs have already separated substantially from each other. Here, the blue cross located at $(0.540, 0.264) (\pi \text{ rad}, \text{a.u.})$, marks the position of hyperbolic point of the primary PO, which has turned unstable. The green circles located at $(0.521, 3.096) (\pi \text{ rad}, \text{a.u.})$, and $(0.562, -2.436) (\pi \text{ rad}, \text{a.u.})$, correspond to the positions of the elliptic fixed points of the newly emerged stable PO. This secondary PO corresponds to a 1:2 resonance ($\omega_R = 2\omega_\theta$). Each of the corresponding fixed points is surrounded by a stability region, where the LDs are slow-varying functions, appearing as almost uniform colored sectors on the LD plots. This stable chain of islands is more clearly visible, when the integration time is increased, as concluded by comparison of Figs. 2 and 3, where a computational time 5 times larger has been considered ($\tau = 10^5$ a.u.). This time is more adequate at these low energies because the integration time of Eq. (2) must be larger than the inverse of the Floquet exponent λ_{\pm}^{-1} of the trajectory of interest [23], and then $\tau = 2 \times 10^4$ a.u. seems not to be sufficient. In the center of Fig. 3(b) the hyperbolic point related to the

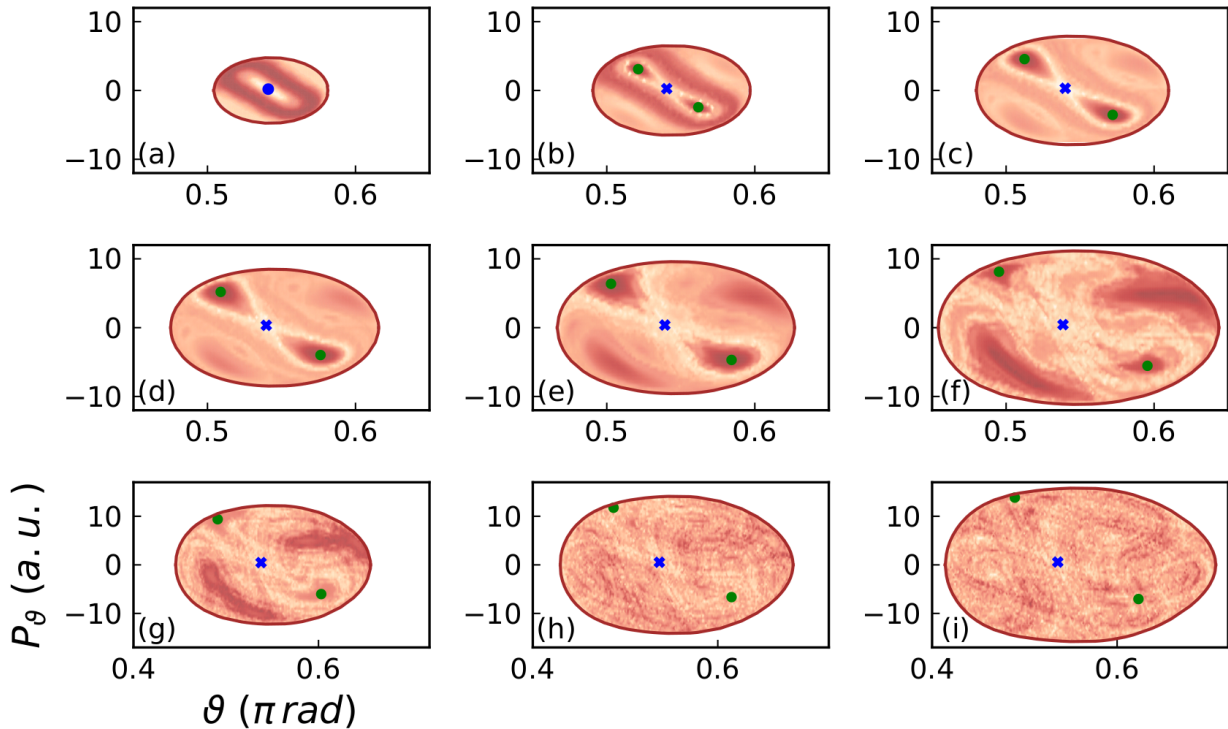


Figure 3: Same as Fig. 3 for $\tau = 10^5$ a.u.

unstable 1:1 PO is located, whose invariant manifolds surround the previous chain of islands. Notice, however, that the hyperbolic character of this PO is only noticeable in its close vicinity, as the distorted tori that surround the 1:1 and 1:2 POs are still present, effectively acting as dynamical barriers. Notice, also, the bright points around the hyperbolic region of Fig. 3(b), which correspond to a new set of elliptic points that emerge because of the occurrence of other bifurcations, as prescribed by the Poincaré-Birkhoff theorem [7].

For $E = 125 \text{ cm}^{-1}$, the results of Figs. 2(c) and 3(c) show that the elliptic green fixed points move further apart from the central hyperbolic blue cross. Furthermore, the size of the stability islands increase. Conversely, the size of the outer invariant tori decreases, as prescribed by the Kolmogorov-Arnold-Moser theorem [7, 36]. For $E = 145 \text{ cm}^{-1}$, from visual inspection of Figs. 2(d) and 3(d), one concludes that the size of the stable islands has noticeably increased. For $E = 185 \text{ cm}^{-1}$, the LD plots shown in Figs. 2(e) and 3(e) present many more details. In this case, the LDs change more significantly because of the presence of invariant manifolds filling the region of phase space where the motion is chaotic.

For a vibrational energy of $E = 250 \text{ cm}^{-1}$, as considered in Figs. 2(f) and 3(f), new structures can be recognized. The size of the region presenting chaotic motion has further increased, while the size of the regions of regular motion, characterized by a large value in the LDs and a dark color in the plots, reduces. This behavior is also observed for $E = 300 \text{ cm}^{-1}$ in Figs. 2(g) and 3(g), $E = 400 \text{ cm}^{-1}$ in Figs. 2(h) and 3(h), and $E = 500 \text{ cm}^{-1}$ in Figs. 2(i) and 3(i), respectively. In all these cases, the dynamics in most of the accessible phase space is dominated by the invariant manifolds that emerge from the central 1:1 resonance. Notice that for all these higher energies, as well as other larger ones, the integration time of $\tau = 2 \times 10^4$ a.u. considered in Fig. 2 seems to be more adequate than that of $\tau = 10^5$ a.u. used in Fig. 3 to identify the invariant manifolds that emerge from the central stretch PO. The reason lies on the stability of this PO, which has a larger characteristic stability exponent, so its inverse is smaller.

1. Bifurcation scheme for low energies

To provide a more comprehensive qualitative analysis of phase-space structural changes at low energies, we show in Fig. 4 the trace value of the transversal monodromy matrix $\mathcal{M}_1^\perp(T)$ with respect to the vibrational energy, for both (a) the central 1:1 resonance, and (b) the outermost 1:2 resonance. Here, the horizontal lines highlight some of the values

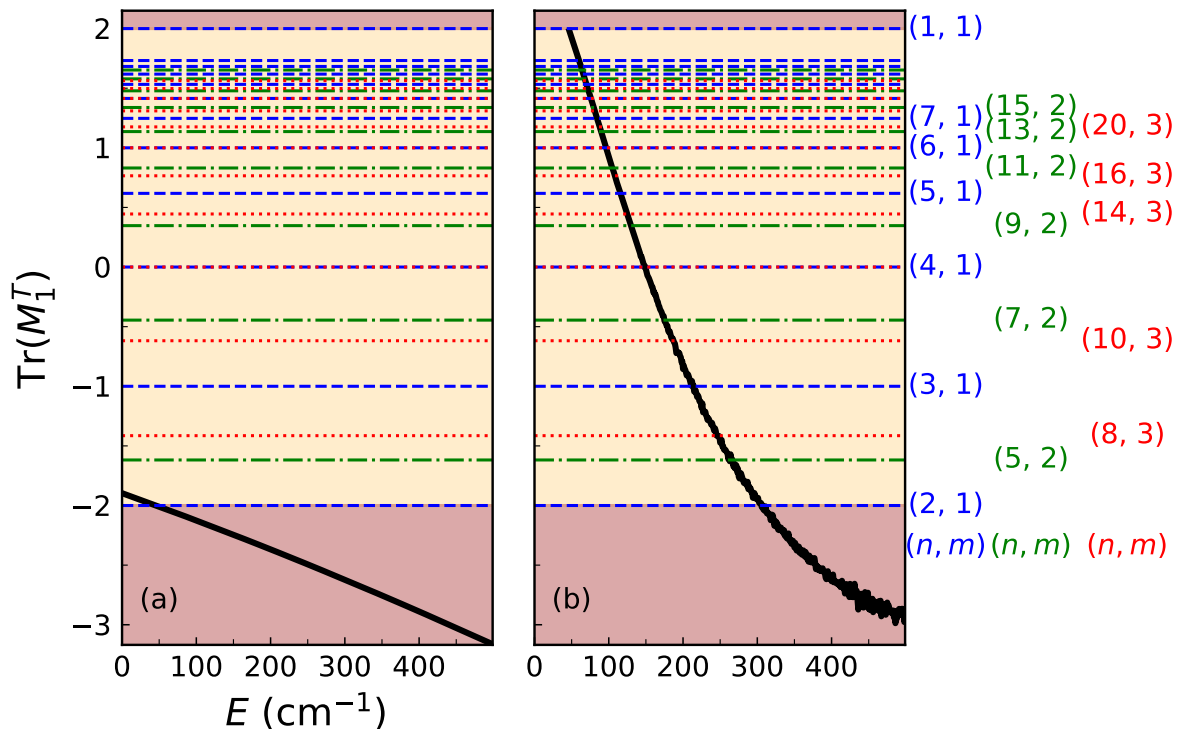


Figure 4: Trace of the monodromy matrix as a function of the vibrational energy for (a) the central 1:1 periodic orbit, and (b) the outmost 1:2 periodic orbit. The orange central and the redish regions correspond to stable and unstable behavior, respectively. The horizontal lines mark some of the positions where the bifurcation condition given by Eq. (6) is satisfied for $n = 1$ (dashed blue), $n = 2$ (dotted-dashed green), $n = 3$ (dotted red). The first (n, m) values appear on the right-hand side of the plot. The corresponding bifurcation energies are listed in Table I.

where the trace fulfills Eq. (6) for $n = 1$ (dashed blue), $n = 2$ (dotted-dashed green), and $n = 3$ (dotted red). Some of the (n, m) pairs can be found on the right-hand side of the figure. These pairs of numbers approximately correspond to the quantization numbers of the most regular molecular eigenstates [37]. The combinations that yield the same trace value as those involving lower integers, e.g. $(n, m) = (4, 2)$ (equivalent to $(n, m) = (2, 1)$) and $(n, m) = (9, 3)$ (equivalent to $(n, m) = (3, 1)$), have been omitted.

Initially, we observe that the 1:1 resonance is stable for vibrational energies below the bifurcation threshold $E_{\text{bifur},1}^{\text{min}} = 45.9 \text{ cm}^{-1}$, where a bifurcation $(n, m) = (1, 1)$ takes place. Conversely, energies surpassing $E_{\text{bifur},1}^{\text{min}}$, render the 1:1 resonance unstable, as the trace value monotonically decreases with the energy (at least within the range considered). We identify the corresponding invariant manifolds through LDs, visually discerned in Figs. 2(e)-2(i) and 3(b)-3(d).

Second, when the vibrational energy equals $E_{\text{bifur},1}^{\text{min}}$, the previous 1:1 resonance becomes marginally stable. Then, an additional 1:2 resonance degenerated with the 1:1 resonance emerges. The trace value of the corresponding transversal monodromy matrix also decreases on average with some small oscillations. The 1:2 resonance remains stable (orange central region) for energies below $E_{\text{bifur},2}^{\text{min}} = 308.4 \text{ cm}^{-1}$ and unstable for energies above $E_{\text{bifur},2}^{\text{min}}$ (redish region), where a bifurcation $(n, m) = (2, 1)$ occurs. This finding is consistent with the presence of the stable islands in Figs. 2(b)-2(g) and 3(b)-3(g), and with their absence in Figs. 2(h)-2(i) and 3(h)-3(i). The 1:2 resonance also experiences infinite series of bifurcations within the range $(E_{\text{bifur},1}^{\text{min}}, E_{\text{bifur},2}^{\text{min}})$. Some examples of the corresponding bifurcating energies are listed in Table I.

B. Phase-space structures for high energies

Figure 5 shows the LD plots for energies above the energetic barrier located at $\theta = \pi \text{ rad}$, which equals $V(\pi, R_{\text{MEP}}(\pi)) = 939.6 \text{ cm}^{-1}$. As shown in Fig. 5(a), which corresponds to $E = 1000 \text{ cm}^{-1}$, most of the acces-

Table I: Energies in cm^{-1} , where the bifurcation condition (6) for n -period periodic orbits with $n = 1, 2, \dots, 10$ (left) for the resonance 1:2 located close to the absolute minimum of the potential, and (right) for the resonance 1:1 that is localized close to the saddle point located at the top of the energetic barrier $\theta = \pi$ rad. All accessible values of m are considered. The positions marked with a hyphen (–) provide the same results as other combinations of (n, m) .

n	m (Resonance 1:2 close to the minimum)			m (Resonance 1:1 close to the right saddle point)		
	1	2	3	1	2	3
1	45.9	–	–	1343.2	–	–
2	308.4	–	–	4220.6	–	–
3	211.8	–	–	3453.5	–	–
4	148.1	–	–	2723.7	–	–
5	115.7	262.7	–	2287.5	3922.5	–
6	96.5	–	–	2022.6	–	–
7	84.3	174.6	286.1	1853.0	3044.5	4065.2
8	76.0	–	246.2	1738.9	–	3766.1
9	70.1	129.9	–	1658.8	2477.3	–
10	65.8	–	187.0	1600.5	–	3170.8

sible phase space is located around the potential absolute minimum, as in Figs. 2 and 3. However, the motion is in this case essentially governed by the invariant manifolds associated with the stretch POs that are placed at the top of the energetic barrier located at $\theta = \pi$ rad, as discussed in detail elsewhere [24]. These manifolds, and not those of the two POs introduced in the previous section, appear automatically as continuous lines in the LD plots, showing their importance for the global vibrational dynamics of the molecule. Notice, also, the presence of the corresponding homoclinic tangle that is responsible for the highly nonlinear dynamics. Likewise, recall that the energetically accessible area of the phase space is much smaller in the neighborhood of the previous POs than around the potential minimum. This difference lies on the fact that in the vicinity of the barrier top most of the mechanical energy is potential, while around the potential minimum it is mostly kinetic energy.

When the vibrational energy of the molecule surpasses the energy $E = 1494 \text{ cm}^{-1}$ of the main barrier that is located at $\theta \approx 0.55\pi$ rad, the motion can also take place around the relative minimum located at $\theta = 0$ rad. This fact can be inferred from inspection of Figs. 5(b)-(f), where the LD plots for vibrational energies equal to (b) 1500 cm^{-1} , (c) 2000 cm^{-1} , (d) 2500 cm^{-1} , (e) 3000 cm^{-1} , and (f) 3500 cm^{-1} are shown. As mentioned above within the discussion of Fig. 5(a), the invariant manifolds that emerge from the PO with $\vartheta \approx \pi$ rad, become also visible in all cases considered, which confirms their dramatic impact on the molecular dynamics. Nevertheless, the invariant manifolds associated with an additional stretch PO located at $\theta \approx 0.55\pi$ rad make the dynamics much more involved due to the occurrence of a heteroclinic tangle formed with the already existing invariant manifolds. The changes in the vibrational energy yield also changes in the stability of the PO, and in the invariant manifolds. In fact, as discussed in more detail below, a new region of stability around $\theta = \pi$ rad emerges at $E_{\text{bifur},1}^{\text{SP}} = 1343.2 \text{ cm}^{-1}$, which manifests as an increasing-size light area around $(\vartheta, P_{\vartheta}) = (\pi \text{ rad.}, 0 \text{ a.u.})$ in the LD plots introduced in Figs. 5(b)-(f).

1. Bifurcation scheme for high energies, and the stabilization around the secondary energetic barrier

In order to study in more detail the stabilization observed around the secondary energetic barrier located at $\theta = \pi$ rad, we analyze here the stability of the bifurcating PO that is found in that region, and the phase-space evolution in its neighbourhood when the vibrational energy is tuned.

First, in order to identify the precise value of the bifurcation energy, where the stability region emerges, we show in Fig. 6 the value of the trace of the monodromy matrix of the PO located at $\theta \approx \pi$ rad as a function of the vibrational energy. Here, we have also marked with horizontal lines the positions where the bifurcation condition (6) is fulfilled along with some of the n and m indices. As can be seen, the value of $\text{Tr}(\mathcal{M}_1^{\perp})$ monotonically decreases with the energy within the considered range. At the saddle-point energy (939.65 cm^{-1}) the trace of the monodromy matrix is $\text{Tr}(\mathcal{M}_1^{\perp}) \approx 2.61$, a value that is larger than 2, so, according to the theory outlined in Sec. III B 1, it is associated with an unstable PO. For $E_{\text{bifur},1}^{\text{SP}} = 1343.2 \text{ cm}^{-1}$, the unstable PO suffers a bifurcation and turns marginally stable as $\text{Tr}(\mathcal{M}_1^{\perp}) = 2$. At this point, both eigenvalues (5) of the monodromy matrix are equal to 1, and the stable manifold degenerates with the unstable manifold. For energies only slightly larger than $E_{\text{bifur},1}^{\text{SP}}$, three stretch POs are visible. The central PO is stable, while the two POs on its left- and right-hand sides are unstable, being organized in a V-shape that is symmetrical respect to the $\theta = \pi$ rad axis. (Recall that only one of them is included in the fundamental domain

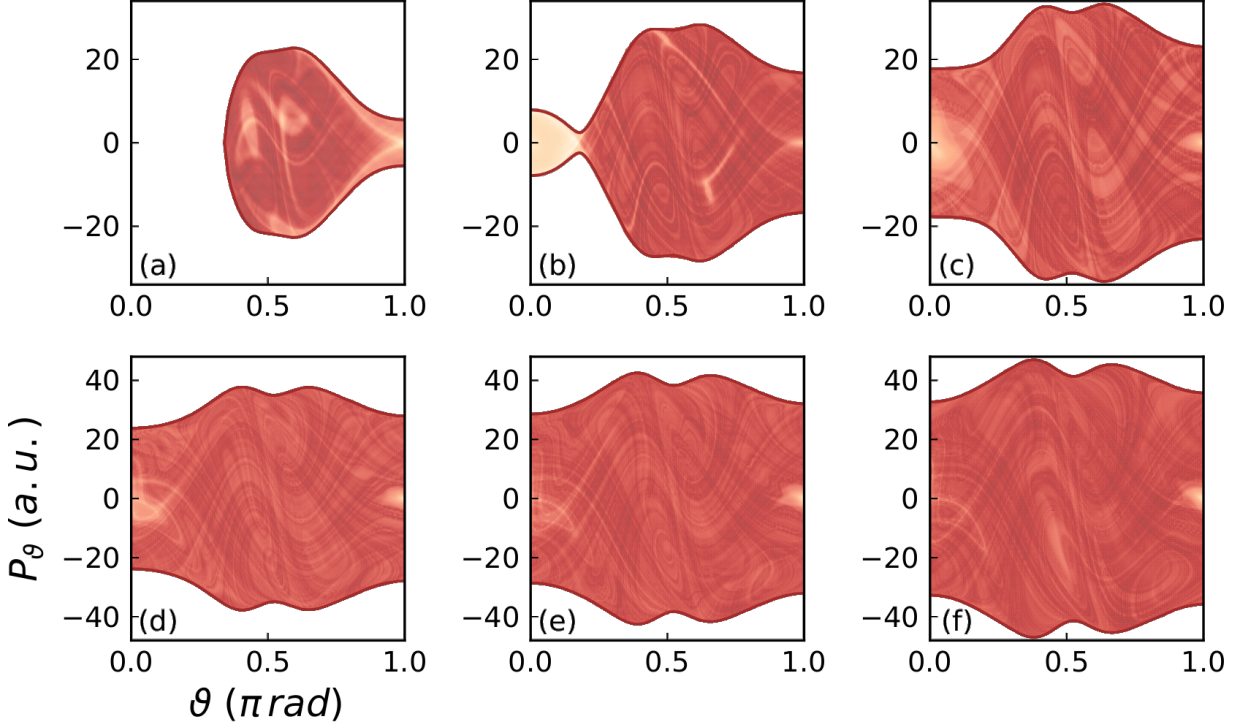


Figure 5: Same as Fig. 2 for vibrational energies equal to (a) 1000 cm^{-1} , (b) 1500 cm^{-1} , (c) 2000 cm^{-1} , (d) 2500 cm^{-1} , (e) 3000 cm^{-1} , and (f) 3500 cm^{-1} .

$0 \leq \theta \leq \pi$ rad.) All these POs correspond to resonances with $(n, m) = (1, 1)$, in agreement with the results predicted by the bifurcation theory shown in Table I and Fig. 6.

The imprint of the bifurcation on the phase-space structure is also remarkably captured by the LDs, as shown in Fig. 7, where the LDs (2) computed solely backwards (left) and forward (middle) in time along with their sum (right) are shown. Within the linear region, the manifolds are aligned with the eigenvectors of the monodromy matrix. The maximal slope of the eigenvectors, i.e., of the manifolds in the neighborhood of the PO, is obtained at the saddle point energy, and then decreases. Notice that for $E = 940 \text{ cm}^{-1}$ (a value only slightly larger than the potential energy at the saddle point) the two manifolds are almost linear lines that coincide with the diagonals of the top panels in Fig. 7. As the energy increases, the central region of the manifolds gets distorted and folds, and the slope of the manifolds reduces, as inferred from the comparison of the previous results with those corresponding to $E = 1100 \text{ cm}^{-1}$ (second row), and $E = 1200 \text{ cm}^{-1}$ (third row). At the bifurcation energy, the two manifolds coincide at the center with the horizontal axis, and degenerate, as shown in the figure (fourth row). At this point, the original hyperbolic point in the LD plots stabilizes and turns into a parabolic point. As the energy further increases, e.g. for $E = 1500 \text{ cm}^{-1}$ shown in the bottom line of Fig. 7, this parabolic point transforms into a central elliptic point and two hyperbolic points at both sides of it. A new stability region surrounds the elliptic point. The motion within this region is separated from the rest of the phase space as it is confined by the invariant manifolds that emerge from the two novel hyperbolic points. These manifolds act as true separatrices for the dynamics. From a global perspective, the elliptic point corresponds to a stable PO, and two hyperbolic points to two unstable POs.

Figure 8 shows the sum of the forward and backwards LDs for higher energies. As can be seen, the two hyperbolic points separate from the central elliptic point with the energy, this increasing the size of the stability island. Similarly, the corresponding unstable POs move apart from the central stable PO. In order to unveil the new structures that emerge within this region, we show in Fig. 9 the LD plots for the same energies but computed up to a time of $\tau = 10^9$ a.u. Here, a more detailed view of the region surrounding the stable PO is achieved. Notice, in particular, the 6 islands that are visible in Fig. 9(d) due to the bifurcation $(n, m) = (6, 1)$ that takes place for a vibrational energy of 2022.6 cm^{-1} , and the 4 islands shown in Fig. 9(d) that emerge when the $(n, m) = (4, 1)$ bifurcation happens for a vibrational energy of 2723.7 cm^{-1} (see Table I).

For higher energies, the PO remains stable until $E_{\text{bifur},2}^{\text{SP}} = 4220.6 \text{ cm}^{-1}$, where it experiences another bifurcation

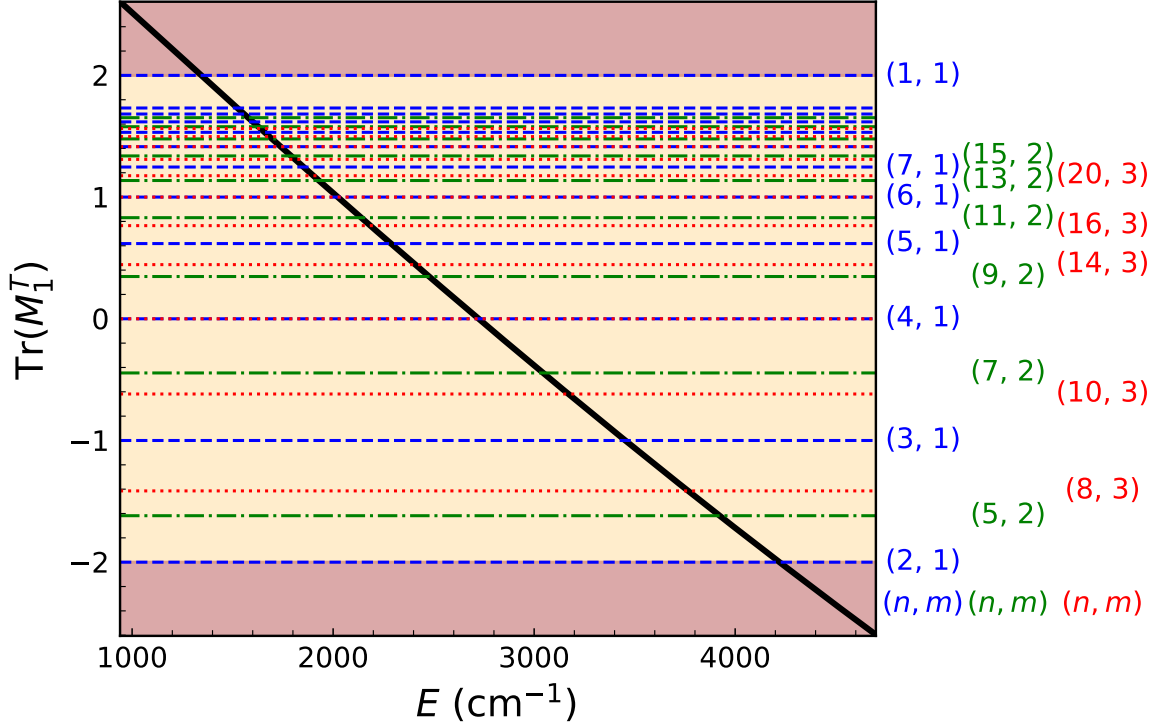


Figure 6: Same as Fig. 4 for the stretch periodic orbit that is found at $\theta \approx \pi$ rad, which is stable within the range $1343.2\text{cm}^{-1} < E < 4220.6\text{cm}^{-1}$.

turning into a 1:2 unstable PO because $\text{Tr}(\mathcal{M}_1^\perp) = -2$ (see Fig. 6). Notice the presence of a structure forming an angle of $\sim 80^\circ$ with the horizontal axis for $E < E_{\text{bifur},2}^{\text{SP}}$ in Figs. 10(a)-(e). For $E = E_{\text{bifur},2}^{\text{SP}}$, these structures collapse, as shown in Fig. 10(f), where a novel ∞ -shaped structure is observed. This ∞ -shaped structure is formed by the invariant manifolds of the stretch PO that is located at the center of the plot. Moreover, it circumvents a stability region, where a 1:2 resonance is placed. Likewise, as the energy further increases, the size of this stable region increases, as shown in 10(g), 10(h), and 10(i) related to $E = 4300\text{cm}^{-1}$, $E = 4400\text{cm}^{-1}$, and $E = 4500\text{cm}^{-1}$, respectively (see Ref. [39] for further details).

To conclude, we show in Fig. 11 the LD plots for vibrational energies equal to (a) 4600cm^{-1} , (b) 4700cm^{-1} , and (c) 4800cm^{-1} . Moreover, in order to assess the accuracy of these computations, we also present in the bottom panels of Fig. 11 an explicit calculation of the invariant manifolds by, first, diagonalizing of the corresponding transversal monodromy matrix, and, second, calculating a composite PSS (7) related to the time-propagation of a large set of 10^4 initial conditions located on the stable and unstable manifolds, respectively. Figure 11(d) shows the results for the stable manifold, and Fig. 11(e) for the unstable manifold. Notice the wild oscillations of the manifolds [24], caused by the strong anharmonicities in the PES, which are responsible for the highly nonlinear molecular dynamics. The agreement between the explicitly computed invariant manifolds and the LDs results is better observed when comparing Fig. 11(c) with Fig. 11(f), where the previous manifolds have been superimposed.

V. SUMMARY

In this work, the phase-space structures of KCN molecular system have been analyzed using Lagrangian descriptors. For low energies, the motion surrounds the minimum of the potential energy surface. In this situation, the motion is regular due to the presence of invariant tori, a fact that is detected by the Lagrangian descriptors computed over a characteristic Poincaré surface of section of the system. As the energy increases, the structure of the phase space changes dramatically. On the one hand, invariant tori breakdown as predicted by the Kolmogorov-Arnold-Moser theorem. On the other hand, a series of bifurcations take place. We have observed that the Lagrangian descriptors correctly account for all these changes if a sufficiently long integration time is considered.

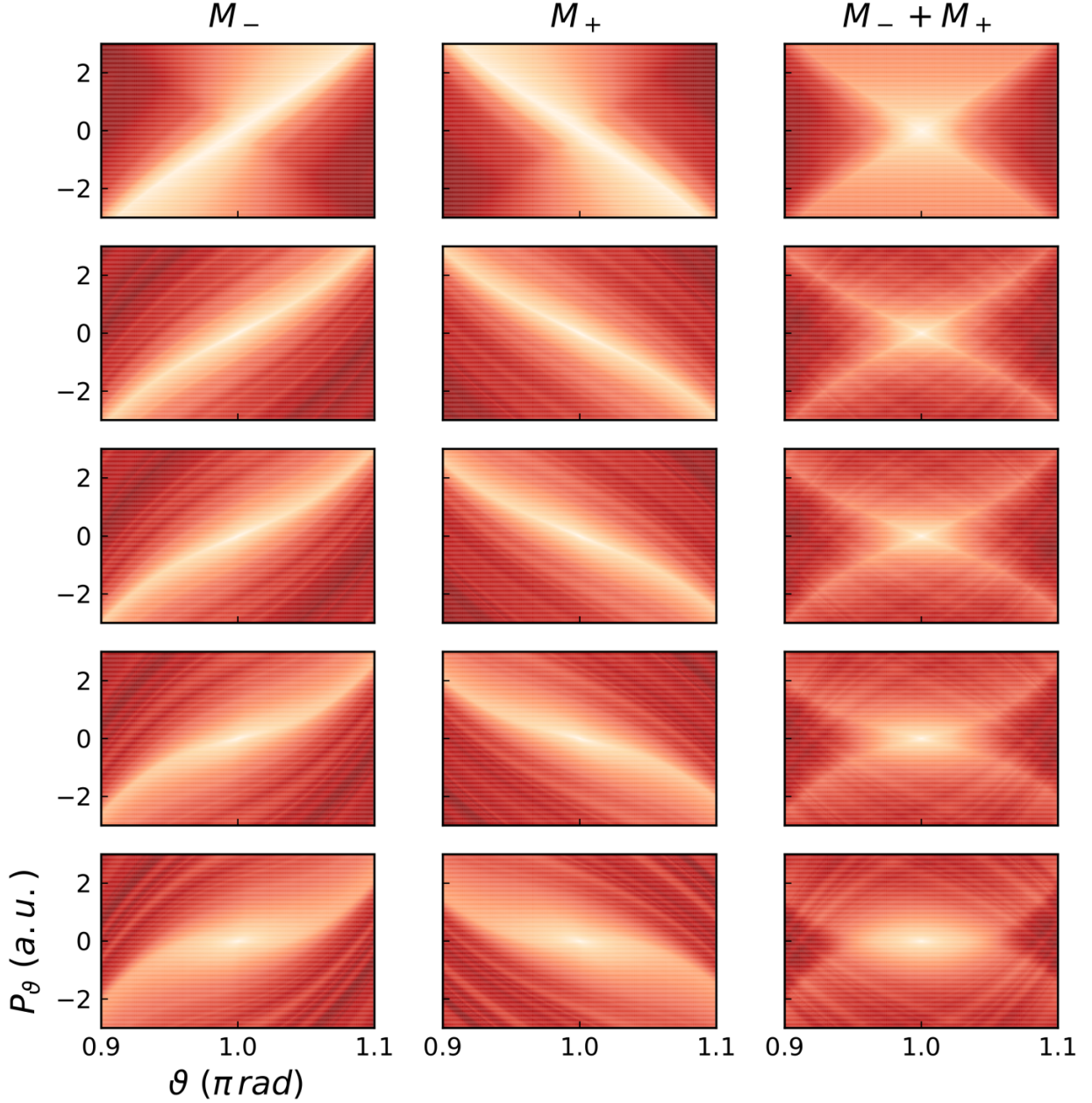


Figure 7: Lagrangian descriptors (2) computed backwards (left), M_- , and forwards (middle), M_+ , in time, and their sum, $M_- + M_+$, for $\tau = 2 \times 10^4$ a.u., and $p = 0.4$, and vibrational energies equal to (from top to bottom) 940 cm^{-1} , 1100 cm^{-1} , 1200 cm^{-1} , $E_{\text{bifur},1}^{\text{SP}} = 1343.2 \text{ cm}^{-1}$, and 1500 cm^{-1} .

For energies above that of the saddle point located at $\theta = \pi \text{ rad}$ but below the energy of the saddle point found at $\theta = 0.55\pi \text{ rad}$, the motion is essentially by the invariant manifolds that emerge from the unstable 1:1 periodic orbits located at $\theta \approx \pi \text{ rad}$. We arrive at this conclusion because the plots of the Lagrangian descriptors show up automatically as continuous lines these manifolds (and not others). Furthermore, these invariant manifolds also give rise to the emergence of a stable region at the top of the energetic barrier. At the center of this stable region, a 1:1 resonance can be found, which experience a series of bifurcations, which have a clear imprint on the phase space. We have shown that the stability analysis of the central periodic orbit correctly predicts the bifurcation energies.

For energies that surpass the energy of the saddle point found at $\theta = 0.55\pi \text{ rad}$, the dynamics much more involved due to the occurrence of a heteroclinic tangle because of the interactions between the invariant manifolds associated

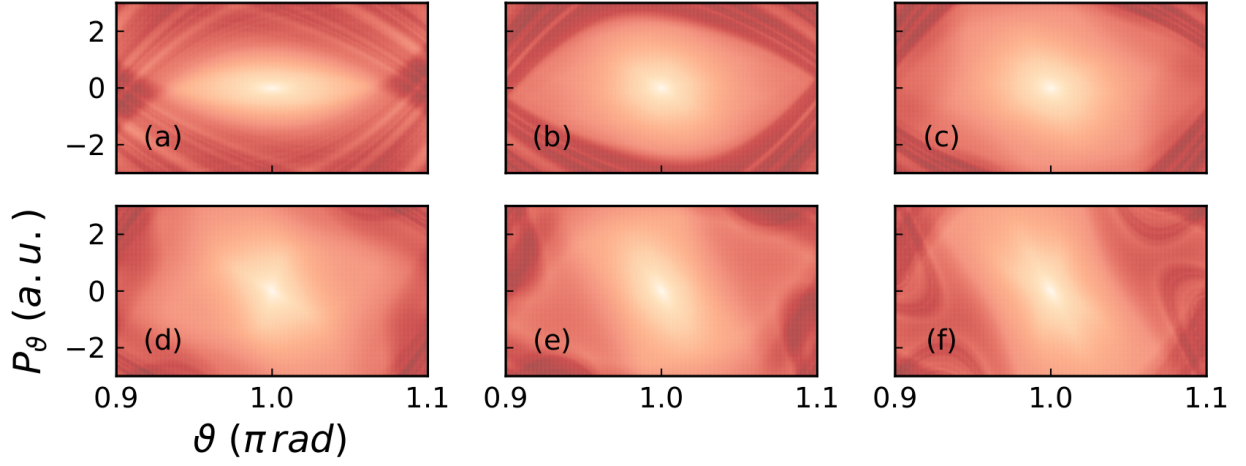


Figure 8: Same as Fig. 2 for vibrational energies equal to (a) 1600 cm^{-1} , (b) 2000 cm^{-1} , (c) 2400 cm^{-1} , (d) 2800 cm^{-1} , (e) 3200 cm^{-1} , and (f) 3600 cm^{-1} .

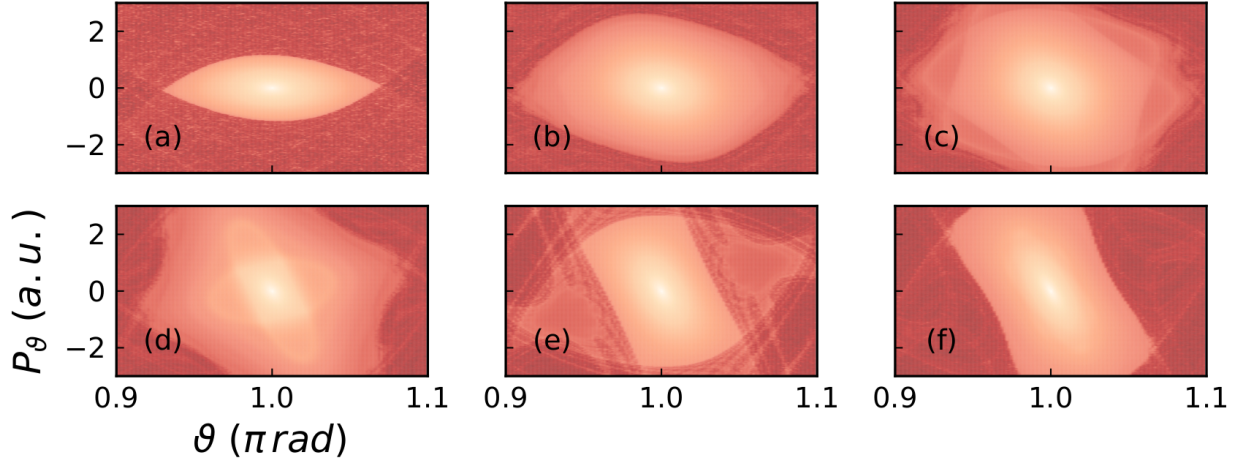


Figure 9: Same as Fig. 8 for $\tau = 10^5 \text{ a.u.}$

with the periodic orbits that are located at the top of the energetic barriers, surrounding the corresponding saddle points.

ACKNOWLEDGEMENTS

This work has been partially supported by the Grant PID2021-122711NB-C21 funded by MCIN/AEI/10.13039/501100011033. The authors also acknowledge computing resources at the Magerit Supercomputer of the Universidad Politecnica de Madrid.

[1] Cvitanović, P., Artuso, R., Mainieri, R. Tanner, G. and Vattay, G. (2016), *Chaos: Classical and quantum*, Niels Bohr Institute: Copenhagen.

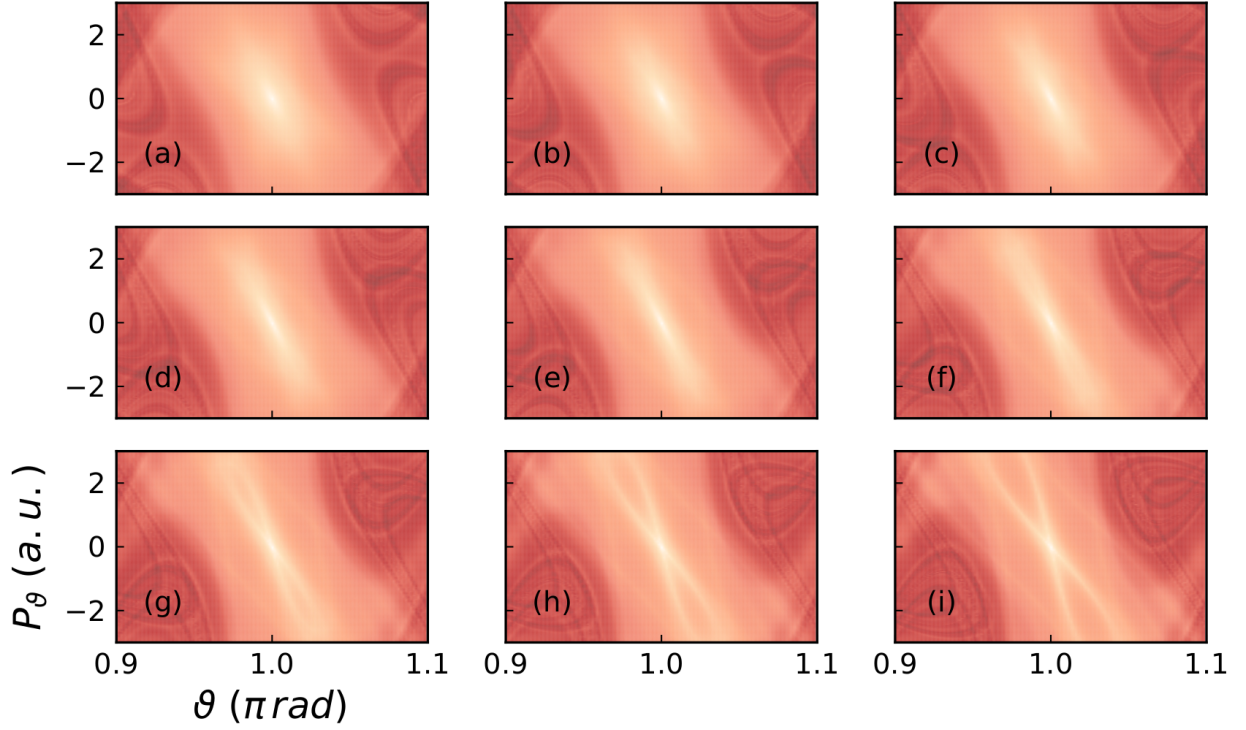


Figure 10: Same as Fig. 7 for vibrational energies equal to (a) 3700 cm^{-1} , (b) 3800 cm^{-1} , (c) 3900 cm^{-1} , (d) 4000 cm^{-1} , (e) 4100 cm^{-1} , (f) 4220.6 cm^{-1} , (g) 4300 cm^{-1} , (h) 4400 cm^{-1} , and (i) 4500 cm^{-1} .

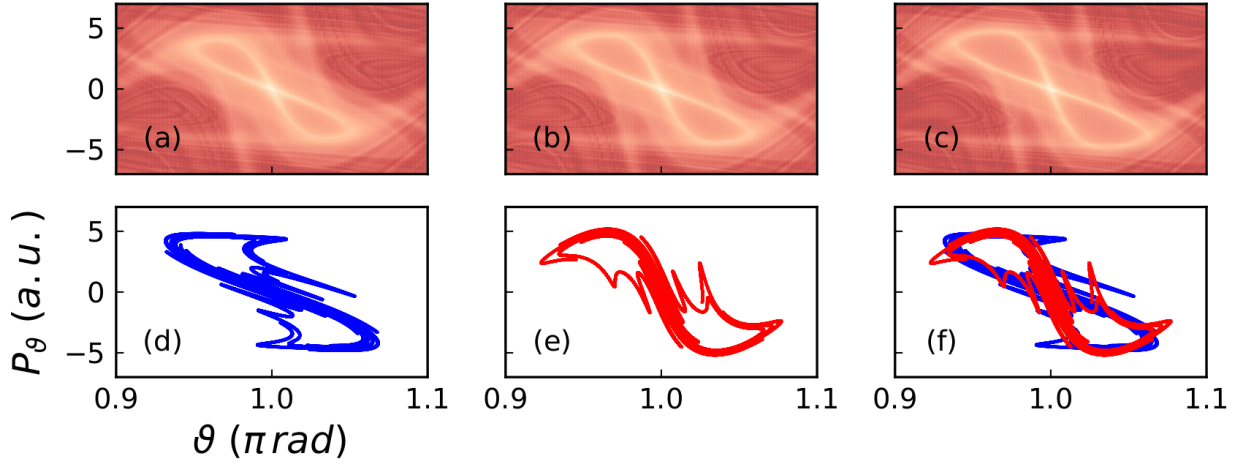


Figure 11: Same as Fig. 7 for vibrational energies equal to (a) 4600 cm^{-1} , (b) 4700 cm^{-1} , and (c) 4800 cm^{-1} , and (d) stable, and (e) unstable invariant manifolds of the stretch periodic orbit located at the top of the energetic barrier found at $\theta = \pi$ rad separated, and (f) superimposed for 4800 cm^{-1} .

- [2] Celletti, A. (2010), *Stability and chaos in celestial mechanics*, Springer praxis books, 1st ed, Springer-Verlag: Berlin, Heidelberg, New York.
- [3] Katok, A. and Hasselblatt, B. (1995), *Introduction to modern theory of dynamical systems*, Cambridge University Press: Cambridge.
- [4] Hale, J. and Koçak, H. (1991), *Dynamics and bifurcations*, Springer-Verlag: New York.

- [5] Lakshmanan, M. (1996), *Chaos in Nonlinear Oscillators: Controlling and Synchronization*, World Scientific Series on Nonlinear Science Series A: Volume 13, World Scientific: Singapur.
- [6] Kambe, T. (2004), *Geometrical theory of dynamical systems and fluid flows*, Advances Series in Nonlinear Mechanics, Vol. 23, World Scientific: Singapore.
- [7] Lichtenberg, A. J. and Leiberman, M. A. (2010), *Regular and stochastic motion*, Applied Mathematical Sciences, vol. 38, Springer-Verlag: New York.
- [8] Froeschlé, Cl., Gonczi, R., and Lega, E. (1997), The fast Lyapunov indicator: a simple tool to detect weak chaos. Application to the structure of the main asteroidal belt, *Planet Space Sci.* **45**, 881-6.
- [9] Froeschlé, C. and Lega, E. (2000), n the structure of symplectic mappings. The Fast Lyapunov indicator: a very sensitive tool, *Celestial Mech. Dynam. Astronom.* **78**(1), 167-95.
- [10] Skokos, C. (2001), Alignment indices: a new, simple method for determining the ordered or chaotic nature of orbits, *J. Phys. A* **34**(47), 10029-43.
- [11] Benitez, P., Losada, J.C., Benito, R.M. and Borondo, F. (2015), Using the small alignment index chaos indicator to characterize the vibrational dynamics of a molecular system: LiNC-LiCN, *Phys. Rev. E* **92**, 042918.
- [12] Cincotta, P. M. and Simó, C. (2000), Simple tools to study global dynamics in non-axisymmetric galactic potentials - I, *Astron. Astrophys. Suppl. Ser.* **147**(2), 205-28.
- [13] Cincotta, P. M., Giordano, C. and Simó C. (2003), Phase space structure of multi-dimensional systems by means of the mean exponential growth factor of nearby orbits, *Physica D* **182**(3), 151-78.
- [14] Jiménez-Madrid, J. A. and Mancho, A. M. (2009), Distinguished trajectories in time dependent vector fields, *Chaos* **19**(1), 013111.
- [15] Lopesino, C. Balibrea-Iniesta, F. Wiggins, S. and Mancho, A. M. (2015), Lagrangian descriptors for two dimensional, area preserving, autonomous and nonautonomous maps, *Commun. Nonlinear Sci. Numer. Simul.* **27**(1), 40-51.
- [16] Mancho, A. M. Wiggins, S. Curbelo, J. and Mendoza, C. (2013), Lagrangian descriptors: A method for revealing phase space structures of general time dependent dynamical systems, *Commun. Nonlinear Sci. Numer. Simul.* **18**(12), 3530-57.
- [17] Mendoza, C. and Mancho, A. M. (2010), Hidden Geometry of Ocean Flows, *Phys. Rev. Lett.* **105**, 038501.
- [18] Darwish, A., Norouzi, S., Di Labbio, G. and Kadem, L. (2021), Extracting Lagrangian coherent structures in cardiovascular flows using Lagrangian descriptors, *Phys. Fluids* **33**(11), 111707.
- [19] Craven, G. T. and Hernandez, R. (2015), Lagrangian descriptors of thermalized transition states on time-varying energy surfaces, *Phys. Rev. Lett.* **115**, 148301.
- [20] Pandey, P., Naik and S. Keshavamurthy, S. (2022), Influence of low frequency modes on dynamical concertedness in double proton transfer dynamics, *Commun. Nonlinear Sci. Numer. Simul.* **109**, 106326.
- [21] Forlevesi, M. D., Egydio de Carvalho, R. and de Lima, Emanuel F. (2023), Lagrangian descriptor and escape time as tools to investigate the dynamics of laser-driven polar molecules, *Phys. Rev. E* **107**, 024209.
- [22] Revuelta, F., Benito, R.M. and Borondo, F. (2019), Unveiling the chaotic structure in phase space of molecular systems using Lagrangian descriptors, *Phys. Rev. E* **99**, 032221.
- [23] Revuelta, F., Benito, R.M. and Borondo, F. (2021), Identification of the invariant manifolds of the LiCN molecule using Lagrangian descriptors, *Phys. Rev. E* **104**, 044210.
- [24] Revuelta, F., Arranz, F. J., Benito, R. M. and Borondo, F. (2023) Unraveling the highly nonlinear dynamics of KCN molecular system using Lagrangian descriptors, *Commun. Nonlinear Sci. Numer. Simul.* **123**, 107265.
- [25] Carlo, G. G. and Borondo, F. (2020), Lagrangian descriptors for open maps, *Phys. Rev. E* **101**, 022208.
- [26] Simile Baroni, R. and de Carvalho, R. Egydio (2024), Lagrangian descriptors: The shearless curve and the shearless attractor, *Phys. Rev. E* **109**, 024202.
- [27] Zimper, S., Ngapasare, A., Hillebrand, M., Katsanikas, M., Wiggins, S. R. and Skokos, Ch. (2023), Performance of chaos diagnostics based on Lagrangian descriptors. Application to the 4D standard map, *Physica D* **453**, 133833.
- [28] Carlo, G. G., Montes, J. and Borondo, F. (2022), Lagrangian descriptors for the Bunimovich stadium billiard, *Phys. Rev. E* **105** 014208.
- [29] Arnaut, L. (2021), *Chemical Kinetics*, Elsevier: Amsterdam.
- [30] Wales, D. J. (2003), *Energy landscapes*, Cambridge University Press: Cambridge.
- [31] Atkins, P., de Paula, J. and Keeler, J. (2006), *Physical Chemistry*, 11th ed., Oxford University Press: Oxford.
- [32] Ma, J. (2005), Usefulness and Limitations of Normal Mode Analysis in Modeling Dynamics of Biomolecular Complexes, *Structure* **13**(3), 373-380.
- [33] Marx, D. and Hutter, J. (2009), *Ab initio molecular dynamics: basi theory and advanced methods*, Cambridge University Press: Cambridge.
- [34] Uzer, T., Jaffé, C., Palacián, J., Yanguas, P. and Wiggins, S. (2002), The geometry of reaction dynamics, *Nonlinearity* **15**(4), 957-92.
- [35] Birkhoff, G. D. (1913), Proof of Poincaré's geometric theorem, *Trans. Am. Math. Soc.* **14**, 14.
- [36] Arnold, I., Gusein-Sade, S. M. and Varchenko, A. N. (2006), *Mathematical aspects of classical and celestial mechanics*, Springer-Verlag: Berlin, Heidelberg.
- [37] Párraga, H., Arranz, F. J., Benito, R. M. and Borondo, F. (2013), *Ab initio* potential energy surface for the highly nonlinear dynamics of the KCN molecule, *J. Chem. Phys.* **139**(19), 194304.
- [38] F. Borondo, E. Fontich and P. Martín (2024), Chaotic scattering of He atoms off a Cu surface with corrugated Morse potential, arXiv preprint available at <https://arxiv.org/abs/2401.05795>.
- [39] Párraga, H., Arranz, F. J., Benito, R. M. and Borondo, F. (2018), Above saddle-point regions of order in a sea of chaos in the vibrational dynamics of KCN, *J. Phys. Chem. A* **122**, 3433-41.